Shear strain tunable exciton dynamics in two-dimensional semiconductors

Xiaofei Liu* and Wanlin Guo†
State Key Laboratory of Mechanics and Control of Mechanical Structures,
Key Laboratory for Intelligent Nano Materials and Devices of Ministry of Education,
Nanjing University of Aeronautics and Astronautics, Nanjing 210016, China

(Received 8 July 2018; revised manuscript received 12 November 2018; published 2 January 2019)

Inhomogeneous strain effects on exciton dynamics have become particularly attractive with the emergence of two-dimensional flexible semiconductors. However, a solid understanding of the shear strain effect is lacking. Here, we study tunable exciton dynamics in two-dimensional semiconductors that have inhomogeneous shear strain. The state-of-the-art first-principles calculations based on the GW plus Bethe-Salpeter equation formalism show that in monolayer molybdenum disulfide, an isotropic semiconductor, the exciton excitation energy can be dramatically tuned as an even function of shear strain with a deformation potential of -50 meV/1%, despite the induced anisotropy of optical absorption with respect to the polarization direction of incident light. For an anisotropic semiconductor such as phosphorene, the modulation of exciton excitation energy is found to be shear-direction dependent. The finite-element simulations further reveal a shear-induced funnel effect of excitons in a micrometer scale MoS_2 disk. The enhanced understanding of inhomogeneous strain engineering presented in this study has the potential to be instrumental in the design of novel optoelectronic devices.

DOI: 10.1103/PhysRevB.99.035401

I. INTRODUCTION

Strain engineering, which focuses on modulating materials' electronic performance by strains, has played a crucial role in the semiconductor industry [1–4]. One exceptional strategy of strain engineering, originating in the 1970s, applies an inhomogeneous strain field for the confinement of excitons [5,6]. In recent years, due to the unprecedented elastic tolerance and flexibility of mechanical loading in reduced dimensions, more attention is being directed at the inhomogeneous strain engineering of low-dimensional flexible semiconductors [7–14]. Fu *et al.* and Han *et al.* demonstrated through experiment and theoretical investigation that the tensile strain gradient in bent semiconductor nanowires gives rise to a flexoelectronic effect [15–17]. Using first-principles calculations, Feng *et al.* proposed a funnel effect of excitons in monolayer molybdenum disulfide (MoS_2) with inhomogeneous biaxial strains. This was subsequently confirmed by experiments [18,19]. Furthermore, San-Jose *et al.* predicted an inverse funnel effect in few-layered black phosphorus [20]. Those novel inhomogeneous strain effects will likely be instrumental in the design of optoelectronic devices.

The underlying mechanism of inhomogeneous strain engineering is to drive the center-of-mass motion of excitons via the spatially varying exciton excitation energy modulated by inhomogeneous strain field. Until now, strains applied to the inhomogeneous strain engineering of two-dimensional (2D) semiconductors have been mainly biaxial or uniaxial tensions/compressions [21,22]. This is because the materials' band gap can be modulated through the stretching and compression of covalent bonds [23,24]. Shear strain, another typical mechanical deformation that distorts the shape of lattice but preserves the unit cell volume, has rarely been exploited for inhomogeneous strain engineering, even as the shear strain gradient has been critical in the pseudomagnetism of graphene [25,26]. Given that shear and tensile strains always coexist in practical inhomogeneous strain fields because of the compatibility conditions for strains [27], it is urgent to explore the shear strain tunable exciton dynamics in 2D semiconductors.

In this work, we present a comprehensive theoretical study of inhomogeneous shear strain engineering in representative 2D semiconductors, isotropic monolayer MoS_2, and anisotropic phosphorene. State-of-the-art first-principles calculations based on the GW plus Bethe-Salpeter equation (BSE) formalism are used to reveal two distinctive shear effects in monolayer MoS_2. First, the tuning of the quasiparticle (QP) gap is an even function of the shear strain, in marked contrast to the effect of the biaxial strain. The deformation potential of excitons is calculated to be -50 meV/1%, comparable to that in low-dimensional semiconductors under biaxial or uniaxial strains [17,18]. Second, shear strains induce an optical anisotropy with respect to the polarization direction of incident light. For phosphorene, the modulation of exciton excitation energy is also shear-direction dependent, as is similarly the case in its uniaxial strain engineering [20,28]. To highlight the exceptional function of shear strain in inhomogeneous strain engineering, a shear-induced funnel effect of excitons in a micrometer scale MoS_2 disk without hydrostatic strain is presented through exciton dynamics simulations.

II. SIMULATION DETAILS

The prerequisite for investigating the strain tunable exciton dynamics is to obtain the profile of exciton excitation energy in strain fields. According to the formulation in continuum mechanics, a 2D strain tensor can

*liuxiaofei@nuaa.edu.cn
†wlguo@nuaa.edu.cn

be decomposed into three independent components, as $\varepsilon = \varepsilon_{\text{biaxial}} + \varepsilon_{\text{shear1}} + \varepsilon_{\text{shear2}}$, where $\varepsilon_{\text{biaxial}}$ stands for the 2D hydrostatic deformation, $\varepsilon_{\text{shear1}} = \begin{pmatrix} 0 & \varepsilon_{12} \\ \varepsilon_{12} & 0 \end{pmatrix}$ and $\varepsilon_{\text{shear2}} = \begin{pmatrix} (\varepsilon_{11} - \varepsilon_{22})/2 & 0 \\ 0 & -(\varepsilon_{11} - \varepsilon_{22})/2 \end{pmatrix}$ correspond to the shear deformations. The deformation potentials of excitons under those strains can be individually calculated using state-of-the-art first-principles theories. Then, the potential energy at any given strain can be approximated by adding up the contributions from its three components. Here, the mean-field eigenstates were calculated with the local density approximation (LDA) and norm-conserving pseudopotentials, using QUANTUM ESPRESSO [29–31]. The self-energy correction was carried out with the one-shot G_0W_0 approach as implemented in BERKELEYGW [32,33]. In the calculation of inverse dielectric matrices, ∼900 unoccupied bands were included, using k grids of $15 \times 15 \times 1$ for MoS_2 and $9 \times 12 \times 1$ for phosphorene. To calculate the excitation spectra including electron-hole $(e - h)$ interactions [34], six highest valance bands and six lowest conduction bands were included in the BSE calculations, with the k grids for MoS_2 and phosphorene being increased to $30 \times 30 \times 1$ and $18 \times 24 \times 1$, respectively. In all calculations, a vacuum slab of 25 Å was used to avoid any spurious interaction between periodic images. A slab truncation of Coulomb potential was also employed. The spin-orbit interaction was not considered because it is inessential for a qualitative understanding of strain engineering [18].

III. RESULTS AND DISCUSSIONS

A. Shear strain effect on the band structure of MoS_2

We focus on the electronic structures of monolayer MoS_2 modulated by shear strains, since the biaxial strain effects have been well documented [18,21,35,36]. Figures 1 and 2 illustrate the QP band structures along the k paths in the deformed Brillouin zone and the contour plots of the topmost valance band. In strain-free MoS_2, the QP direct gap at the Brillouin zone corners $K+/K-$ is 2.91 eV, consistent with a previous study [37]. The band dispersion at the Brillouin zone center Γ is isotropic, while that at $K+/K-$ is threefold symmetric. Upon the application of $\varepsilon_{\text{shear1}}$, a significant rhomboidal warping of the band dispersion at Γ is observed. As a consequence of this warping, the effective hole mass at Γ is reduced along the 45° direction but increased along the −45° direction. At $K+/K-$, the threefold symmetry of band dispersion is broken by $\varepsilon_{\text{shear1}}$, but the hole mass along the 45° direction is increased instead. Those anisotropic electrical conductances stem from the shear-induced tension and compression in the two orthogonal directions. The other strain component $\varepsilon_{\text{shear2}}$, a pure shear deformation in a coordinate system rotated by 45°, actually corresponds to a tension along the x axis and a compression of identical amplitude along the y axis, giving rise to an elliptical warping of the band dispersion at Γ [Fig. 2(e)]. Likewise, $\varepsilon_{\text{shear2}}$ modulates the hole masses at Γ and $K+/K-$ anisotropically. The shear induced electronic anisotropy would not only be useful to improve the carrier motilities in 2D semiconductors as has been utilized in the strained silicon [38] but also contributes to an optical anisotropy as shown below.

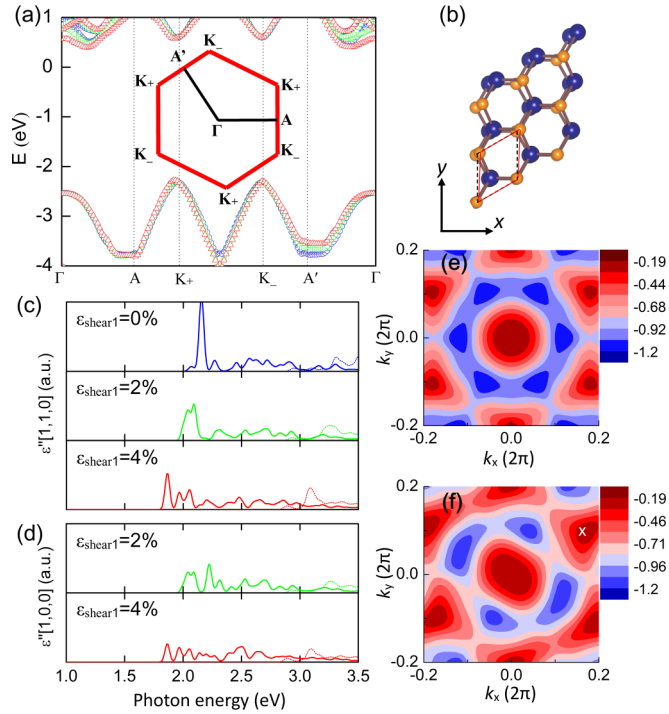

FIG. 1. (a) Quasiparticle band structures of monolayer MoS_2 under $\varepsilon_{\text{shear1}}$ of 0% (circle), 2% (square), and 4% (triangle). The inset illustrates the k paths in the first Brillouin zone. (b) Illustration of the shear deformation $\varepsilon_{\text{shear1}}$. The dashed rhombus and the solid rhomboid represent the pristine and deformed unit cells, respectively. (c),(d) Optical absorption spectra with incident light polarized along the armchair [1,1,0] and zigzag [1,0,0] directions, calculated using a Gaussian broadening of 20 meV. The solid and dotted curves correspond to the spectra with and without $e - h$ interactions. The spectra for negative $\varepsilon_{\text{shear1}}$ are not shown, as the crystal structures under $\pm\varepsilon_{\text{shear1}}$ are identical upon a mirror symmetry transformation. (e),(f) Contour plots of the topmost valance bands in the strain-free and $\varepsilon_{\text{shear1}} = 4\%$ cases. The $K+$ point in (f) is marked by a cross.

In the studied range of shear strain, the gap around $K+/K-$ remains narrower than that at Γ, determining the direct gap of MoS_2. Figures 3(a) and 3(b) show the direct gaps along the depicted k paths as a function of shear strain. Under $\varepsilon_{\text{shear1}}$, the gaps around both $K+$ and $K-$ decrease with increased strain amplitude. Because of the mirror symmetry between the crystal structures under $\pm\varepsilon_{\text{shear1}}$, the gaps are an even function of $\varepsilon_{\text{shear1}}$. In the case of $\varepsilon_{\text{shear2}}$, the gaps around $K+$ and $K-$ decrease and increase with positive $(\varepsilon_{11} - \varepsilon_{22})/2$, respectively, and vice versa with negative $(\varepsilon_{11} - \varepsilon_{22})/2$. Nevertheless, the overall direct gap is still an even function of $\varepsilon_{\text{shear2}}$, posing a marked contrast to the strain engineering by biaxial strain. It is worth mentioning that while the LDA gap without self energy correction is underestimated by ∼ 1.2 eV, the relative change of gap with shear strain can be well described by the mean-field theory.

B. Shear strain effect on the optical absorption spectra of MoS_2

Figure 1(c) displays the optical absorption spectra of monolayer MoS_2, calculated with incident light polarized along the armchair direction [1,1,0]. In the strain-free case, we

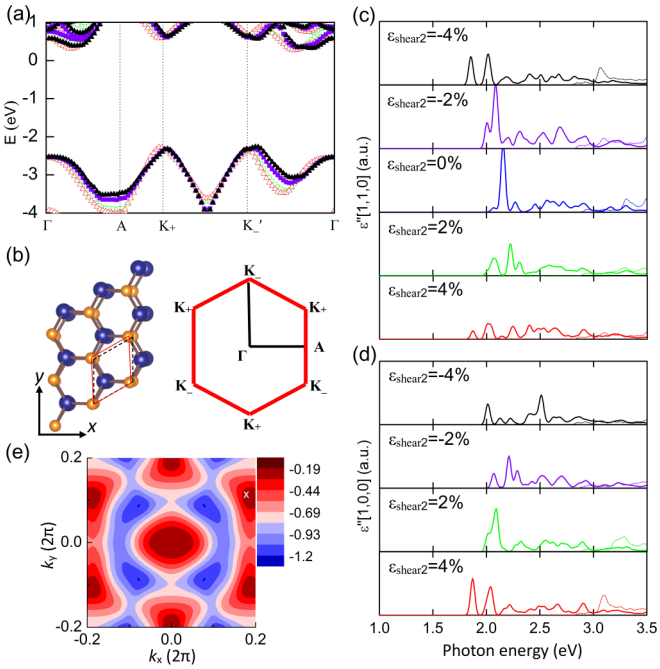

FIG. 2. (a) Quasiparticle band structures of monolayer MoS_2 under ε_{shear2}, with $(\varepsilon_{11}$-$\varepsilon_{22})/2$ of -4% (solid triangle), -2% (solid square), 2% (open square), and 4% (open triangle). (b) Illustrations of the deformed unit cell and the first Brillouin zone. (c),(d) Optical absorption spectra with incident light polarized along the armchair [1,1,0] and zigzag [1,0,0] directions, calculated using a Gaussian broadening of 20 meV. (e) Contour plot of the topmost valance band under $(\varepsilon_{11}$-$\varepsilon_{22})/2 = 4\%$. The $K+$ point is marked by a cross.

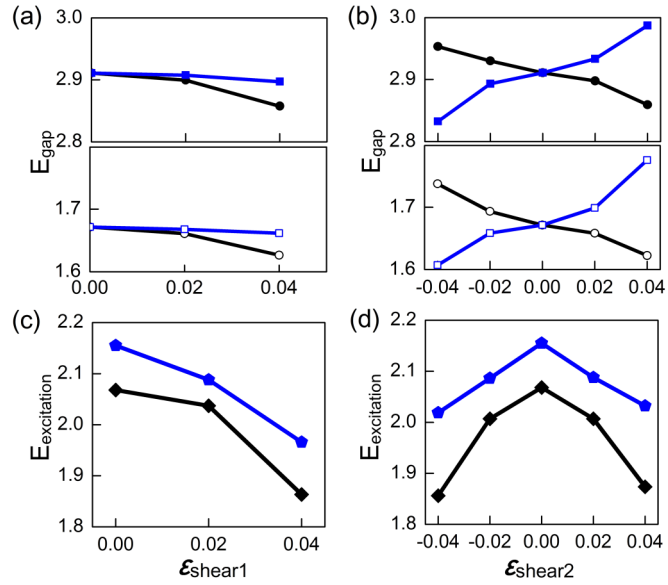

FIG. 3. (a) Direct gap of monolayer MoS_2 along the k paths depicted in Fig. 1 as a function of ε_{shear1}. The gaps around $K+$ and $K-$ are labeled by the circle and square. The solid and open scatters correspond to the G_0W_0 and LDA results, respectively. (b) Direct gap of monolayer MoS_2 along the k paths depicted in Fig. 2 as a function ε_{shear2}. (c),(d) Excitation energy of the lowest (diamond) and next lowest (pentagon) absorption peaks as a function of ε_{shear1} and ε_{shear2}. As the local maximums/minimums deviate from $K+/K-$, the change of gap shown in (a),(b) is less significant than the shift of excitation energy shown in (c),(d).

observe the lowest energy absorption peak without $e-h$ interactions at 2.96 eV, which corresponds to optical transitions at $K+/K-$. In the G_0W_0-BSE spectrum taking into account $e-h$ interactions, the energy level of this absorption peak is significantly reduced to 2.06 eV, due to the weak Coulomb screening in the reduced dimension and resultant large exciton binding energy [39]. Moreover, another absorption peak next to the lowest one is located at 2.15 eV. According to a previous study [37], the two absorption peaks can be attributed to the bound exciton formed from transitions at the $K+/K-$ valleys and its first excited state, respectively. We note that while the positions of the two peaks are close but not identical to the accurate ones [37] converged with 6000 bands and a k grid of $72 \times 72 \times 1$, the relative change of the peak position under strain as tested for the biaxial case [Fig. S2] complies with the previous theoretical report [18,40]. There are also absorption peaks near 2.5 eV, which may be assigned to the intricate C peak that is quite sensitive to momentum space sampling. Figure S1(a) presents the optical absorption spectrum of strain-free MoS_2 calculated with incident light polarized along the zigzag [1,0,0] direction [40]. Since MoS_2 is intrinsically isotropic, the optical spectra with different incident light coincide precisely with each other.

The application of shear strain ε_{shear1} in monolayer MoS_2 gives rise to a significant redshift of the absorption peak. As shown in Fig. 1(c), the energy levels of the two lowest peaks at $\varepsilon_{shear1} = 4\%$ are reduced to 1.86 and 1.96 eV, indicating that shear strain gradients can be used to drive the motion of excitons as biaxial strain gradients do. A distinct shear strain effect absent in biaxial strain engineering is the induction of optical anisotropy with respect to the polarization direction. With incident light polarized along $[-1, 2, 0]$, $[-2, 1, 0]$, or $[1, -1, 0]$ [Fig. S1(b)], the two lowest energy peaks are significantly diminished, accompanied with the rise of higher-energy peaks near 2.50 eV [40]. Despite the induced anisotropy, the spectra polarized along the zigzag [1,0,0] direction [Fig. 1(d)] show the same redshift of the absorption peak under ε_{shear1}.

As shown in Figs. 2(c) and 2(d), ε_{shear2} also leads to the redshift of the absorption peak. However, special care must be taken to determine the position of the lowest energy peak. While redshifts of the two lowest peaks under $(\varepsilon_{11}$-$\varepsilon_{22})/2 = 2\%$ can be observed in the G_0W_0-BSE spectrum with light polarized along the zigzag direction [1,0,0], the electronic transition corresponding to the lowest energy peak cannot be excited by light polarized along the armchair direction [1,1,0]. This is due to the induced optical anisotropy. Similarly, under $(\varepsilon_{11}$-$\varepsilon_{22})/2 = -2\%$ or -4%, the lowest energy peak cannot be found in the spectra with light polarized along [1,0,0].

To calculate the driving force that can be exerted on excitons by shear strain gradients, the energies of the two lowest excitation peaks are presented as a function of shear strain in Figs. 3(c) and 3(d). In spite of the optical anisotropy and polarization-direction dependence discussed above, the exciton excitation energies of both ε_{shear1} and ε_{shear2} can be thought of as even functions of shear strain. Regardless of the shear direction, the average deformation potential for the

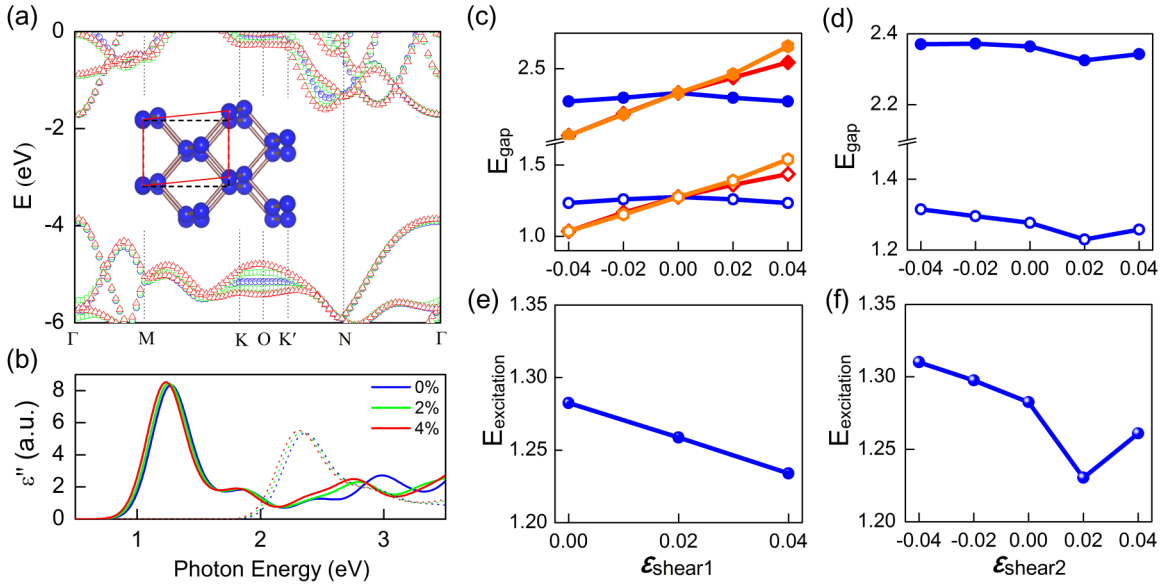

FIG. 4. (a) Quasiparticle band structures of phosphorene under $\varepsilon_{\text{shear1}}$ of 0% (circle), 2% (square), and 4% (triangle). (b) Optical absorption spectra with incident light polarized along the armchair direction, calculated using a Gaussian broadening of 100 meV. (c) Direct gaps at Γ as a function of $\varepsilon_{\text{shear1}}$ (blue circles) and uniaxial strains (red diamonds and orange hexagons). (d) Direct gap as a function of $\varepsilon_{\text{shear2}}$. The solid and open scatters in (c),(d) correspond to the G_0W_0 and LDA results, respectively. (e),(f) Excitation energy of the lowest absorption peak as a function of shear strain.

two exciton states is estimated to be −50 meV/1%. This tunability of excitation energy is about half that of the biaxial strain in MoS_2 (as shown in Fig. S2 [40]) and even higher than that of the tensile strain in ZnO nanowires [17,18]. As shear strains do not change the volume in the first order, the pronounced shear effect is beyond expectation. Unlike bulk semiconductors such as Ge and Cu_2O where the shear-induced modulation of the band gap is mainly due to the splitting of degenerate bands [5,6], the origin of the shear effect here is actually similar to that of the biaxial strain engineering in 2D semiconductors. Although the unit cell volume is unchanged, there is one pair of Mo-S bonds at a degree of 15° to the direction extended by positive $\varepsilon_{\text{shear1}}$ and two pairs at a degree of 15° to the direction extended by positive $\varepsilon_{\text{shear2}}$. Consequently, the lengths of those covalent Mo-S bonds can respond to the shear strains significantly.

C. Shear strain effect on the optical absorption spectra of phosphorene

Previous studies found that anisotropic 2D semiconductors provide additional options for uniaxial tensile strain engineering, leading to a tensile direction relied gap modulation [28]. The same is true for the shear strain engineering here, as tested in phosphorene, an anisotropic semiconductor with a gap inside the infrared region [41,42]. Figures 4(a) and S6 show that $\varepsilon_{\text{shear1}}$ distorts the rectangular cell of phosphorene into a rhomboid and that it slightly wraps the isoenergy contour [40]. It is interesting that the direct gap at Γ is narrowed by $\varepsilon_{\text{shear1}}$, which is a signal for a funnel effect instead of the previously found inverse funnel effect induced by tensile strains [20]. Meanwhile, as the geometries under $\pm\varepsilon_{\text{shear1}}$ are related by a mirror symmetry transformation, the modulation of exciton excitation energy in phosphorene is an even function of $\varepsilon_{\text{shear1}}$, with a deformation potential of −14 meV/1% [Figs. 4(b) and 4(c)].

$\varepsilon_{\text{shear2}}$ in phosphorene can be decomposed into a tension along the armchair direction and a compression along the zigzag direction, or in reverse. Thus, the modulation of excitation energy is no longer an even function of $\varepsilon_{\text{shear2}}$. Under a negative $(\varepsilon_{11}\text{-}\varepsilon_{22})/2$, the direct gap can be increased. With positive $(\varepsilon_{11}\text{-}\varepsilon_{22})/2$, however, the gap is decreased at $(\varepsilon_{11} - \varepsilon_{22})/2 = 2\%$ but then increased at 4%. The modulation of excitation energy by $\varepsilon_{\text{shear2}}$ is less effective than that by uniaxial strains [Figs. S4 and S5], implying that the effects of the tension and compression along the two orthogonal directions counteract. Furthermore, $\varepsilon_{\text{shear2}}$ can change the relative order of the first and second conduction bands at Γ. At the strain-free and $(\varepsilon_{11}\text{-}\varepsilon_{22})/2 = 4\%$ cases the energies of the two bands differ by 0.81 and 0.83 eV, respectively, whereas with $(\varepsilon_{11}\text{-}\varepsilon_{22})/2 = -4\%$ the energy difference is reduced to 0.20 eV. With further increased amplitude of $(\varepsilon_{11}\text{-}\varepsilon_{22})/2$, the relative order of the bands would be reversed, resulting in a rotation of the preferred conduction direction [28].

D. Exciton dynamics simulation in MoS_2

Exciton dynamics including the generation, diffusion, recombination, and motion of $e - h$ pairs can modulate the optical emission spectrum of 2D semiconductors. To highlight the role of shear effect in inhomogeneous strain engineering, we construct a pure inhomogeneous shear strain field in a micrometer scale MoS_2 disk. With the inner circumference of an elastic plate being clamped, a mechanical torque is applied at the outer circumference of the plate that bolsters the MoS_2 disk [Fig. 5(a)], resulting in shear strains aligned along the circumferential directions. With the aid of the van der Waals interaction at the interface and the great mechanical flexibility of

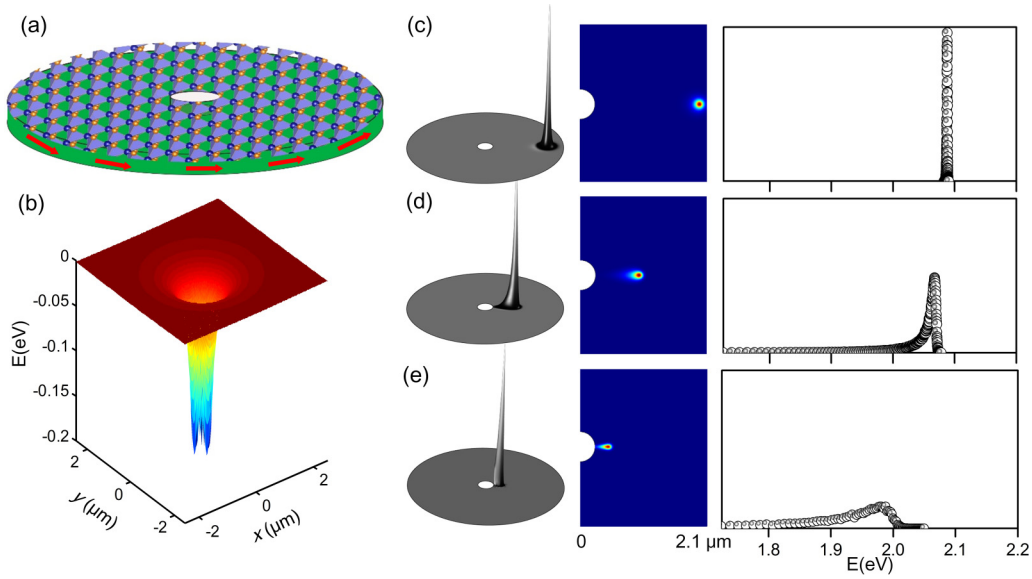

FIG. 5. Exciton dynamics simulations in a micrometer scale MoS_2 disk under an inhomogeneous shear strain filed. (a) Schematic of the MoS_2 disk under the pure shear loading. The outer and inner radii of the disk are 2.5 and 0.25 μm, respectively. (b) Relative potential energy of excitons in the deformed MoS_2 disk. (c), (d) and (e) Height profiles and top views of exciton density. The exciton sources in (c), (d) and (e) locate at a radial distance of 0.5, 1.0 and 2.0 μm, respectively. The normalized exciton densities as a function of energy are shown in the right panels. The excitation energy without strain is calibrated with the average energy of the two lowest peaks.

the atomistic layer, the shear strains in the elastic plate can be transferred to the MoS_2 disk. The shear strain amplitude derived from the mechanical equilibrium condition is related to the radial distance r, as $\varepsilon = cR_{in}^2/r^2$, where R_{in} is the radius of the inner hole. Due to the shear strain gradients, a spatially varying potential for excitons is built up without need of 2D hydrostatic strains, which scales as $E = -E_s R_{in}^2/r^2$. Compared with the indentation-induced centripetal potential [18] that scales as $E = -E_{bi}/r$, the gradients of shear-induced potential at sites far away from the center are milder, but the gradient near the inner circle is much steeper [Fig. 5(b)].

The exciton dynamics were simulated by solving the 2D partial differential equation of diffusion using a finite element method [17]. The shear strain amplitude at the inner circumference was set to 4%, in order to keep the whole strain field within the studied range. The lifetime of excitons and carrier mobility at 20 K were set according to a previous experimental and theoretical study [43], as listed in the Supplemental Material [40]. Constant exciton sources of Gaussian distribution were used to mimic steady optical excitations. A nonflux condition was applied at the boundaries in order to form steady distributions of excitons. As shown in Fig. 5(c), when the exciton source locates far away from the highly strained area at a radial distance of 2.0 μm, the excitons remain localized with a slight spreading originating from free diffusions. As the exciton source moves inwards to $r = 1.0$ or 0.5 μm, the exciton distributions leave a tail pointing to the center. This is a clear evidence in support of exciton concentration or the so-called funnel effect stemming from shear gradients. A novel consequence of the shear-induced funnel effect is the modulation of optical emission spectra. At the low-strain area, a sharp emission peak at 2.09 eV can be observed. At $r = 1.0$ μm, the emission peak will be redshifted by 30 meV and slightly broadened towards the lower-energy side. At $r = 0.5$ μm, the photoluminescence would appear in a broadened energy window wider than 80 meV. Those instances indicate that inhomogeneous shear strains are useful in converting narrow-line incident light into a broad-spectrum emission, as has been realized by inhomogeneous tensile strains [17]. Another merit of the inhomogeneous shear strain field is that the driving force for exciton is centripetal. Thus, when the entire disk is illuminated by sunlight, the excitons stimulated by light of different frequencies and at different sites can be collected around the inner circle, thus contributing to a broad-spectrum harvest of solar energy [18]. Finally, it must be noted that the role of shear strain is not limited to where there are pure inhomogeneous shear strains but may likely be of interest regarding the exciton dynamics under any practical inhomogeneous deformations that present both biaxial and shear components.

IV. CONCLUSIONS

To conclude, we systematically investigated the exceptional shear strain tunable exciton dynamics in 2D semiconductors. In monolayer MoS_2, in spite of the shear-induced optical anisotropy, the exciton excitation energy was dramatically tuned with a deformation potential of up to -50 meV/%. Through exciton dynamics simulations, a shear-induced funnel effect of excitons and a resultant modulation of emission spectra in a micrometer scale MoS_2 disk were demonstrated. In the anisotropic phosphorene, the modulation of exciton energy was found to rely on the shear direction because of the crystal anisotropy. The inhomogeneous shear strain engineering in 2D semiconductors presented here has the potential to be instrumental in the design of novel photovoltaic, photodetection, and photoemitting devices.

ACKNOWLEDGMENTS

This work is supported by National Natural Science Foundation of China (11702132, 51535005, 11772153, and 51472117). X.L. is grateful for the supports from China Postdoctoral Science Foundation (Grants No. 2016M600408 and No. 2017T100362), the Natural Science Foundation of Jiangsu Province (Grants No. BK20170770) and the Research Fund of State Key Laboratory of Mechanics and Control of Mechanical Structures (MCMS-I-0418Y01).

[1] J. Bardeen and W. Shockley, Phys. Rev. **80**, 72 (1950).
[2] A. Lochtefeld and D. A. Antoniadis, IEEE Electr. Device L. **22**, 591 (2001).
[3] M. Ieong, B. Doris, J. Kedzierski, K. Rim, and M. Yang, Science **306**, 2057 (2004).
[4] P. R. Chidambaram, C. Bowen, S. Chakravarthi, C. Machala, and R. Wise, IEEE T. Electr. Device **53**, 944 (2006).
[5] P. L. Gourley and J. P. Wolfe, Phys. Rev. B **20**, 3319 (1979).
[6] D. P. Trauernicht, J. P. Wolfe, and A. Mysyrowicz, Phys. Rev. B **34**, 2561 (1986).
[7] Z. H. Ni, T. Yu, Y. H. Lu, Y. Y. Wang, Y. P. Feng, and Z. X. Shen, ACS Nano **2**, 2301 (2008).
[8] A. Castellanos-Gomez, R. Roldán, E. Cappelluti, M. Buscema, F. Guinea, H. S. J. van der Zant, and G. A. Steele, Nano Lett. **13**, 5361 (2013).
[9] Y. Xu, X. Liu, and W. Guo, Nanoscale **6**, 12929 (2014).
[10] M. Yu, X. Liu, and W. Guo, Phys. Chem. Chem. Phys. **20**, 6374 (2018).
[11] W. Guo and Y. Guo, Phys. Rev. Lett. **91**, 115501 (2003).
[12] C. Lee, X. Wei, J. W. Kysar, and H. James, Science **321**, 385 (2008).
[13] Y. Wei, J. Wu, H. Yin, X. Shi, R. Yang, and M. Dresselhaus, Nat. Mat. **11**, 759 (2012).
[14] A. Castellanos-Gomez, M. Poot, G. A. Steele, H. S. J. van der Zant, N. Agraït, and G. Rubio-Bollinger, Adv. Mat. **24**, 772 (2012).
[15] Q. Fu, Z. Zhang, L. Kou, P. Wu, X. Han, X. Zhu, J. Gao, J. Xu, Q. Zhao, W. Guo, and D. Yu, Nano Res. **4**, 308 (2011).
[16] X. Han, L. Kou, X. Lang, J. Xia, N. Wang, R. Qin, J. Lu, J. Xu, Z. Liao, X. Zhang, X. Shan, X. Song, J. Gao, W. Guo, and D. Yu, Adv. Mat. **21**, 4937 (2009).
[17] X. Fu, C. Su, Q. Fu, X. Zhu, R. Zhu, C. Liu, J. Xu, J. Feng, J. Li, and D. Yu, Adv. Mat. **26**, 2572 (2014).
[18] J. Feng, X. Qian, C. W. Huang, and J. Li, Nat. Photo. **6**, 866 (2012).
[19] H. Li, A. W. Contryman, X. Qian, S. M. Ardakani, Y. Gong, X. Wang, J. M. Weisse, C. H. Lee, J. Zhao, P. M. Ajayan, J. Li, H. C. Manoharan, and X. Zheng, Nat. Commun. **6**, 7381 (2015).
[20] P. San-Jose, V. Parente, F. Guinea, R. Roldán, and E. Prada, Phys. Rev. X **6**, 031046 (2016).
[21] Y. Y. Hui, X. Liu, W. Jie, N. Y. Chan, J. Hao, Y. T. Hsu, L. J. Li, W. Guo, and S. P. Lau, ACS Nano **7**, 7126 (2013).
[22] S. Yang, C. Wang, H. Sahin, H. Chen, Y. Li, S.-S. Li, A. Suslu, F. M. Peeters, Q. Liu, J. Li, and S. Tongay, Nano Lett. **15**, 1660 (2015).
[23] P. Lu, X. Wu, W. Guo, and X. C. Zeng, Phys. Chem. Chem. Phys. **14**, 13035 (2012).
[24] X. Peng, Q. Wei, and A. Copple, Phys. Rev. B **90**, 085402 (2014).
[25] N. Levy, S. A. Burke, K. L. Meaker, M. Panlasigui, A. Zettl, F. Guinea, A. H. C. Neto, and M. F. Crommie, Science **329**, 544 (2010).
[26] F. Guinea, A. K. Geim, M. I. Katsnelson, and K. S. Novoselov, Phys. Rev. B **81**, 035408 (2010).
[27] I. S. Sokolnikoff, *Mathematical Theory of Elasticity* (McGraw-Hill Book Company, New York, 1956).
[28] R. Fei and L. Yang, Nano Lett. **14**, 2884 (2014).
[29] P. Giannozzi *et al.*, J. Phys.: Condens. Matter **21**, 395502 (2009).
[30] P. Hohenberg and W. Kohn, Phys. Rev. **136**, B864 (1964).
[31] We used the pseudopotentials Mo.pz-hgh.UPF, S.pz-hgh.UPF, and P.pz-hgh.UPF from http://www.quantum-espresso.org.
[32] J. Deslippe, G. Samsonidze, D. A. Strubbe, M. Jain, M. L. Cohen, and S. G. Louie, Comput. Phys. Commun. **183**, 1269 (2012).
[33] B. C. Shih, Y. Xue, P. Zhang, M. L. Cohen, and S. G. Louie, Phys. Rev. Lett. **105**, 146401 (2010).
[34] E. E. Salpeter and H. A. Bethe, Phys. Rev. **84**, 1232 (1951).
[35] K. F. Mak, C. Lee, J. Hone, J. Shan, and T. F. Heinz, Phys. Rev. Lett. **105**, 136805 (2010).
[36] A. Splendiani, L. Sun, Y. Zhang, T. Li, J. Kim, C. Y. Chim, G. Galli, and F. Wang, Nano Lett. **10**, 1271 (2010).
[37] D. Y. Qiu, F. H. da Jornada, and S. G. Louie, Phys. Rev. Lett. **111**, 216805 (2013).
[38] S. E. Thompson, G. Sun, Y. S. Choi, and T. Nishida, IEEE T. Electr. Device **53**, 1010 (2006).
[39] J. H. Choi, P. Cui, H. Lan, and Z. Zhang, Phys. Rev. Lett. **115**, 066403 (2015).
[40] See Supplemental Material at http://link.aps.org/supplemental/10.1103/PhysRevB.99.035401 for the supplemental data and the details of the exciton dynamics simulations.
[41] F. Xia, H. Wang, and Y. Jia, Nat. Commun. **5**, 4458 (2014).
[42] V. Tran, R. Soklaski, Y. Liang, and L. Yang, Phys. Rev. B **89**, 235319 (2014).
[43] M. Palummo, M. Bernardi, and J. C. Grossman, Nano Lett. **15**, 2794 (2015).